WP15ER-PR(17) 18392

L Lu et al.

Modelling of radio frequency sheath and fast wave coupling on the realistic ion cyclotron resonant antenna surroundings and the outer wall

Preprint of Paper to be submitted for publication in
Plasma Physics and Controlled Fusion

This work has been carried out within the framework of the EUROfusion Consortium and has received funding from the Euratom research and training programme 2014-2018 under grant agreement No 633053. The views and opinions expressed herein do not necessarily reflect those of the European Commission.

111Equation Chapter 1 Section 1Modelling of radio frequency sheath and fast wave coupling on the realistic ion cyclotron resonant antenna surroundings and the outer wall

L. Lu[1,2,3,a)], L. Colas[1], J. Jacquot[4], B. Després[5], S. Heuraux[2], E. Faudot[2], D. Van Eester[6], K. Crombé[3,6], A. Křivská[6], J-M. Noterdaeme[3,4], W. Helou[1], J. Hillairet[1]

[1]*CEA, IRFM, F-13108 Saint-Paul-Lez-Durance, France*

[2]*IJL, UMR 7198, CNRS-U. de Lorraine, F-54506 Vandoeuvre Cedex, France*

[3]*Department of Applied Physics, Ghent University, Belgium*

[4]*Max-Planck-Institut für Plasmaphysik, EURATOM-Assoziation, Garching, Germany*

[5]*UPMC-Paris VI, Jacques-Louis Lions Laboratory, UMR 7598, Paris, France*

[6]*EURATOM-Belgian State, LPP-ERM-KMS, TEC partner, Brussels, Belgium*

a) *Now at TianQin Research Center for Gravitational Physics, School of Physics and Astronomy, Sun Yat-Sen University, Zhuhai 519082, P. R. China* Email: lulingfeng@mail.sysu.edu.cn

Abstract. In order to model the sheath rectification in a realistic geometry over the size of Ion Cyclotron Resonant Heating (ICRH) antennas, the Self-consistent Sheaths and Waves for ICH (SSWICH) code couples self-consistently the RF wave propagation and the DC SOL biasing *via* non-linear RF and DC sheath boundary conditions (SBCs) applied at plasma/wall interfaces. A first version of SSWICH had 2D (toroidal and radial) geometry, rectangular walls either normal or parallel to the confinement magnetic field $\mathbf{B_0}$ and only included the evanescent slow wave (SW) excited parasitically by the ICRH antenna. The main wave for plasma heating, the fast wave (FW) plays no role on the sheath excitation in this version. A new version of the code, 2D SSWICH-Full Wave, was developed based on the COMSOL software, to accommodate full RF field polarization and shaped walls tilted with respect to $\mathbf{B_0}$. SSWICH-Full Wave simulations have shown the mode conversion of FW into SW occurring at the sharp corners where the boundary shape varies rapidly. It has also evidenced "far-field" sheath oscillations appearing at the shaped walls with a relatively long magnetic connection length to the antenna, that are only accessible to the propagating FW. Joint simulation, conducted by SSWICH-Full Wave within a multi-2D approach excited using the 3D wave coupling code (RAPLICASOL), has recovered the double-hump poloidal structure measured in the experimental temperature and potential maps when only the SW is modelled. The FW contribution on the potential poloidal structure seems to be affected by the 3D effects, which was ignored in the current stage. Finally, SSWICH-Full Wave simulation revealed the left-right asymmetry that has been observed extensively in the strap dissymmetrization experiments, suggesting that the spatial proximity effects in RF sheath excitation, studied for SW only previously, is still important in the vicinity of the wave launcher under full wave polarizations.

1. INTRODUCTION

Ion cyclotron resonant heating (ICRH) is one of the main heating methods in the present-day tokamaks. Waves in the Ion Cyclotron Range of Frequencies (ICRF, 25-100MHz) are launched by phased arrays of poloidal current straps at the Low Field Side of the device and interact firstly with the plasma in the Scrape-Off Layer (SOL). Due to the different mobilities of ions and electrons, the SOL plasma is positively biased with respect to the electrically grounded vessel walls. The DC plasma potential (V_{DC}) mainly occurs across a submillimetric charge separation layer at the plasma-wall interface: the sheath. Radio frequency (RF) waves can induce sheath RF oscillations in their accessible regions. Non-linear rectification of the oscillating RF sheath voltage (V_{RF}) can produce a net enhancement of V_{DC}. Sheath rectification is therefore suspected to reinforce impurity sputtering and heat loads on ICRF antenna surfaces and other plasma facing components. The non-linearity of

the process requires knowing accurately the RF fields that depend on the precise antenna shape and its surroundings. This means taking into account the exact geometries of the antenna structure and of the areas lighted by the wave. The

Better understanding of RF sheaths in tokamaks motivated the development of the Self-consistent Sheath & Waves for Ion Cyclotron Heating (SSWICH) code [Jacquot 2014]. SSWICH couples self-consistently the RF wave propagation and the DC plasma biasing with non-linear sheath boundary conditions (SBC) applied at plasma-facing walls. The first version of the SSWICH code adopted a simple geometry where the confinement magnetic field $\mathbf{B_0}$ was either parallel or perpendicular to the walls. Under such configuration, the RF-SBCs only involved to the slow wave (SW) polarization of the RF fields. The alternative polarization, *i.e.* the Fast Wave (FW), which is the main wave intended to be excited by ICRF antennas, was not accounted for. Its role on the RF sheath excitation remains an open question.

Realistic tokamak walls are shaped and can exhibit any orientation with respect to $\mathbf{B_0}$. Previous studies [D'Ippolito 2008][kohno 2015] have predicted the depolarization of an incoming Fast Wave upon reflection on a tilted wall. The two wave polarizations thus indeed need to be treated simultaneously, and both contribute to the excitation of sheath RF oscillations. Hereafter such process will be called "mode conversion", not to be confused with another coupling of the two polarizations at the ion-ion hybrid resonance.

Besides, during ICRH in AlCATOR C-Mod [Ochoukov 2014] and Tore Supra (TS) [Kubic 2013], enhanced V_{DC} has been observed in remote regions inaccessible to the SW directly excited by the wave launcher. Furthermore, the radial extension of the V_{DC} peak (~3cm) in TS was far larger than the SW radial evanescence length at the measurement location (~5mm) [Kubic 2013]. This was so far interpreted by a DC current transport in the SSWICH-SW code, provided that a phenomenological transverse DC conductivity is correctly adjusted, which is rather uncomfortable [Jacquot2014]. The excitation of so called "far-field" RF sheaths by the fast wave can possibly provide an alternative mechanism to explain this observation, since the region accessible to the Fast Wave is more extended than that for the SW. Indeed, it would be desirable to compare both processes.

On TS, both probe measurements (e.g. [Kubic2013]) and infrared thermography (e.g. [Corre2012]) suggest that sheath effects exhibit a 2-hump poloidal structure with local maxima near the top and bottom of the antenna box. This spatial structure is rather robust and was observed with several antenna types. Previous simulations by SSWICH-SWcould reproduce the measured double-hump structure. This backs the presumption that the RF sheath rectification drives the intense SOL-antenna interactions. But how does the fast wave contribute to this spatial structure?

Lastly, left-right power unbalance experiments of 2-strap arrays on TS [Corre2012] [Colas2013] and ASDEX-Upgrade (AUG) [Bobkov2015] suggest that sheath RF oscillations are enhanced on the antenna side closest to the strap with higher power, while they get attenuated on the opposite side. To understand this left-right asymmetry theoretically, [Colas 2017] suggested that the distance from active or passive radiating elements to the walls might play a role in RF-sheath excitation *via* the SW evanescence. Such "spatial proximity effect" was the guideline for the electrical tuning a 3-strap antenna successfully tested on AUG [Bobkov2017]. We do not know yet how this property evolves in the presence of the evanescent fast wave, whose characteristic evanescence lengths are larger than those of the SW in the SOL region. Even less clear is whether the distance to the wave emitters is still relevant for RF sheath excitation in regions where the waves are

propagative rather than evanescent, or whether alternative kinds of "spatial proximity effects" prevail in these cases.

To address the above questions numerically, section 2 of this paper reports the development of a new SSWICH version (SSWICH-Full Wave) which includes a more realistic antenna geometry, magnetic configuration, wall shape and full wave (fast wave + SW) polarizations. Using the 2D (radial-toroidal) SSWICH-Full Wave code with strap current excitation section 3 explores the role of the fast wave on RF sheath excitation. Similarly section 4 conducts multi-2D SSWICH-Full Wave simulations excited with realistic input field maps of a TS antenna. Section 5 is the conclusion.

1. THE 2D SSWICH-FULL WAVE CODE

To address the questions raised in the introduction, the 2D SSWICH-SW code [Jacquot2014] was extended to a Full-Wave version with shaped walls. This section describes the new tool.

2.1 Specifications and main technical choices in comparison with literature

RF sheath rectification is a stationary non-linear process involving at least the launched RF wave at angular frequency ω_0, coupled non-linearly with DC biasing at zero frequency. In principle, once the system is excited at ω_0, the non-linearity brings up all the harmonics of ω_0 as well. One of the main difficulties in modelling the RF sheath rectification is that the plasma is a time-dispersive medium. So no tractable single dielectric or conductivity tensor is valid for all frequencies. Two strategies are generally followed to solve this problem: either make the problem time dependent (although only the stationary phase is of interest) or coupling several time-harmonic problems with different conductivity tensors.

The first strategy was implemented by Smithe [Smithe 2015]. He uses the method of "auxiliary differential equations", which allows frequency-dependent materials to be treated in the time domain. However his code mainly solves the RF wave propagation in presence of oscillating sheaths. The local plasma DC potentials are inferred in a simple way from the local RF fields by assuming that all sheaths are floating at slow timescales. Over a much smaller domain, Faudot developed a 1D time-dependent fluid model accounting for both RF and DC currents transverse to $\mathbf{B_0}$ [Faudot 2013]. In his method, the plasma conductivity tensor is replaced by a conductivity operator retaining all harmonics.

The rfSOL code [Kohno 2012A], the LPP code [Van Eester 2015] (in reference to Laboratory for Plasma Physics in Brussels) and our SSWICH code follow the second strategy and for simplicity drop the harmonics of the RF frequency. The rfSOL code mainly solves the wave propagation in presence of RF sheaths similar to [Jenkins2015]. The LPP code solves self-consistently the interplay between full wave (fast wave + SW) and plasma density. The fast time scale modifies the density of the slow time scale *via* ponderomotive effects. The SSWICH-Full Wave workflow, sketched in Figure 1, adopts a similar three-module structure as the 2D SSWICH-SW code [Jacquot2014]: the RF part and DC part are solved in different steps using different conductivity tensors. SSWICH code solves propagation of the RF fields **E**, the RF oscillating sheath voltage V_{RF} and the DC plasma potential V_{DC}. These three fields are coupled in a self-consistent loop by non-linear sheath electrical properties. Compared to SSWICH-SW, the modules have been generalized to accommodate full field polarizations and shaped walls.

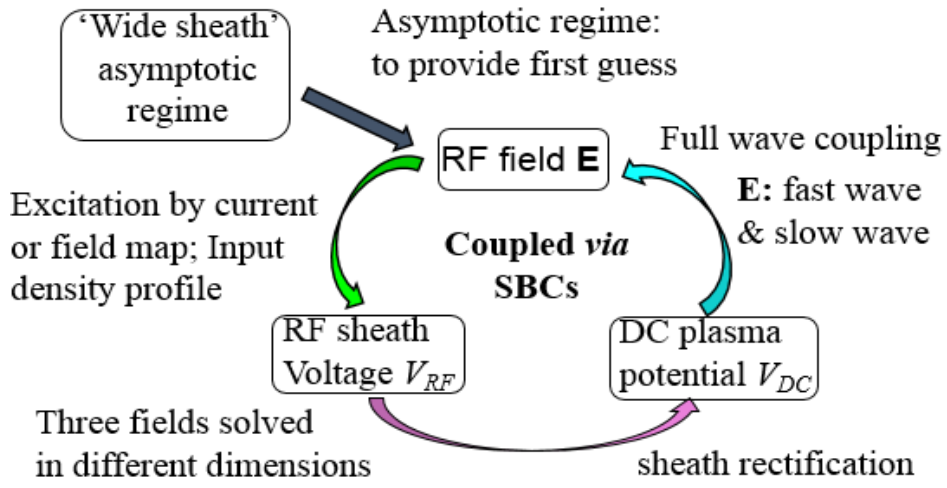

Figure 1. Workflow of the 2D SSWICH-Full Wave code. It's an upgraded version of Fig 5 in [Jacquot 2014]

While Faudot's code and the LPP code presently restrict themselves to a simple geometry with a limited size, our aim is to model the SOL over a realistic antenna size without rescaling. Sheaths are thin (sub-millimetre range) compared to a realistic ICRF antenna with a typical scale of meter, and compared to the typical wavelengths radiated (see e.g. Figure 5 and Figure 7 below). Here we neglected the cross field sheath [Moritz 2016] induced by the difference of Larmor radius between the electrons and ions. In presence of this scale separation it is convenient to treat sheaths as non-linear boundary conditions, as originally proposed in [D'Ippolito2006].

As discussed in the introduction, the orientation of $\mathbf{B_0}$ with respect to the wall influences the wave reflection and the RF sheath excitation. Besides, to interpret the experiments, we would like to investigate the role of geometrical features in antenna and walls for the RF-sheath excitation. Therefore we would like to vary the direction of $\mathbf{B_0}$ and implement shaped material boundaries in the antenna vicinity. In this complex simulation domain the finite element method becomes advantageous. Kohno [Kohno 2012] demonstrated the use of the finite elements for solving plasma wave propagation subject to sheath boundary conditions. This numerical method however imposes using local dielectric tensors. Therefore modelling the non-collisional wave absorption in the hot plasma centre becomes difficult. Our code is implemented using the Finite Element Solver COMSOL.

Given the small-scales to be resolved, especially for the SW, computer resources presently constrain realistic simulation domains to two dimensions, except for [Jenkins 2015]. Kohno simulated a full poloidal cross section in a reference (radial/vertical) plane, surrounded by a shaped vacuum vessel and excited by a sheet of poloidal RF current [Kohno 2015]. In order to implement realistic antenna excitation, our 2D domain, sketched in Figure 2 lies in a toroidal-radial plane, assuming that neither the geometry nor the physical quantities evolve in the third direction (poloidal). Limitations associated to this 2D assumption will be discussed below.

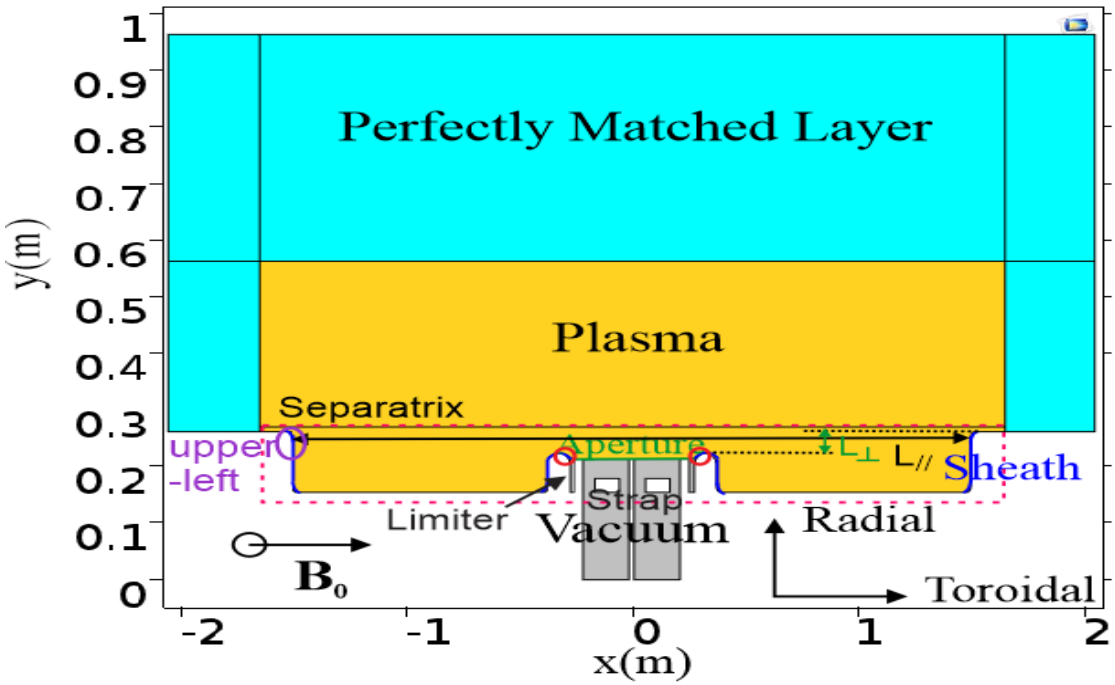

Figure 2. Geometry of the 2D SSWICH-Full Wave simulation domain. x is the toroidal direction, y is the radial direction, the ignored direction z is the poloidal direction of the Tokamak coordinates. Blue curved lines are sheath boundaries; Green horizontal line is the antenna aperture; The red dot rectangle indicates the SOL region whose upper limiter is the Separatrix. The characteristic lengths $L_{//}$ and $L_{\perp}$ are shown in the geometry. Their values are tuned in Figure 9-Figure 10; The upper-left sheath boundary is enclosed by purple circle. $|V_{RF}|$ at this boundary is examined in Figure 9-Figure 10. Two red ellipses surround the curved sheath boundaries where the heat flux is examined in Figure 17

We focus on the antenna vicinity at the low field side of the machine. The simulation domain does not span over the whole radial and toroidal extension of the plasma. But compared to SSWICH-SW, it had to be extended to all regions accessible to the fields radiated by the antenna. It includes the SOL at the Low field side as well as part of the confined plasma. The radial extension is determined to fairly reproduce the power coupling to the core in presence of inhomogeneous plasma with realistic profiles. Contrary to SSWICH-SW, part of the RF fields can access the plasma centre, and thus one needs to attenuate artificially these fields at the inner part of the simulation domain. Here single-pass wave damping will be assumed. For these reasons SSWICH-Full Wave is presently not suited to investigate RF-sheath excitation at the high-field side of a tokamak, due to residual fast waves having crossed the plasma core, as in [Kohno 2015]. Still, SSWICH-Full Wave can study RF sheath excitation at the low field side of the machine, on outer walls remote from the launchers that are inaccessible to the SW directly emitted by the antenna, e.g. the upper left wall circled in purple in Figure 2. In this paper we will call "far-field" these types of sheaths, due to fast waves either directly emitted from the antenna or reflected at the plasma edge before reaching the core. We will compare this "far field" region to "near-field" areas (e.g. red circles on antenna side limiters) accessible to both evanescent FW and SW.

We now detail the different modules of SSWICH-Full Wave.

2.2 RF Wave propagation module

The RF field module solves a time-harmonic vectorial wave equation for the full RF electric field **E**, assumed to oscillate in time as exp(+i$\omega_0 t$) at angular frequency ω_0,

$$\nabla\times(\nabla\times\mathbf{E})-k_0^2\boldsymbol{\varepsilon}_\mathbf{r}\mathbf{E}=0 \qquad 22\backslash^* \text{ MERGEFORMAT ()}$$

In this equation $k_0=\omega_0/c$ is the wave number in vacuum, and one generally adopts a cold plasma dielectric tensor to describe the electrodynamic properties of the fusion plasmas in the regions away from the resonances. The cold plasma dielectric tensor reads,

$$\boldsymbol{\varepsilon}_\mathbf{r}=\begin{pmatrix}\varepsilon_\perp & i\varepsilon_\times & 0\\ -i\varepsilon_\times & \varepsilon_\perp & 0\\ 0 & 0 & \varepsilon_{//}\end{pmatrix}\begin{matrix}\perp 1\\ \perp 2\\ //\end{matrix} \qquad 33\backslash^* \text{ MERGEFORMAT ()}$$

Where three dielectric constants $\varepsilon_\perp$, $\varepsilon_\times$ and $\varepsilon_{//}$, defined in [Stix 1992], vary with the plasma density. Here subscripts ⊥1, ⊥2 and // indicate the two perpendicular directions and the parallel direction with respect to the confinement magnetic field $\mathbf{B_0}$. Compared to [Stix 1992], the signs of the off-diagonal terms change due to the engineering convention we use in this paper. An ICRH antenna can emit two types of cold plasma waves: it is designed to launch mainly the FW, used for core plasma heating, but it also excites parasitically the SW. By substituting the cold plasma dielectric 3 into equation 2 one obtains the dispersion relations of plane waves with these two decoupled polarizations and spatial oscillations as exp $\left(-i\,k_0 n\cdot r\right)$

$$(slow\ wave)\ n_{\perp S}^2=\varepsilon_{//}\left(1-\frac{n_{//}^2}{\varepsilon_\perp}\right) \qquad 44\backslash^* \text{ MERGEFORMAT ()}$$

$$(Fast\ wave)\ n_{\perp F}^2=\frac{(\varepsilon_R-n_{//}^2)(\varepsilon_L-n_{//}^2)}{(\varepsilon_\perp-n_{//}^2)}=\frac{(n_{//}^2-\varepsilon_\perp)^2-\varepsilon_\times^2}{\varepsilon_\perp-n_{//}^2} \qquad 55\backslash^* \text{ MERGEFORMAT ()}$$

Where $\varepsilon_R=\varepsilon_\perp+\varepsilon_\times$, $\varepsilon_L=\varepsilon_\perp-\varepsilon_\times$, $n_{//}$ and $n_\perp$ are the parallel and perpendicular refractive indices, respectively. Under typical tokamak parameters, the SW is almost evanescent everywhere in the Tokamak vacuum vessel. The SW evanescence length is defined as the e-fold decay length,

$$l_{\perp s}=\frac{c}{\omega_0 n_{\perp s}}\approx\frac{c}{\omega_0\sqrt{|\varepsilon_{//}|}}\approx\frac{c}{\omega_{pe}} \qquad 66\backslash^* \text{ MERGEFORMAT ()}$$

Where c the light speed and ω_{pe} the electron plasma frequency. Given the typical TTS SOL density (n_e=10^{18}m^{-3}), the SW has an evanescence length of 5mm. This wave has a notable electric field component that is parallel to $\mathbf{B_0}$. On the contrary, the FW is propagating at the center of the vacuum vessel and it is the main wave to achieve the plasma heating. It has a large electric field that is perpendicular to $\mathbf{B_0}$. For this wave, the wavelength can vary from several centimeters to millimeters. The FW propagating region is separated from the evanescence region by the *R* cut-off layer at the edge. The *R* cut-off

layer is derived by setting $\varepsilon_R = n_{//}^2$ in the FW dispersion relation, Eq. 5. The FW is propagating above the *R* cut-off layer and evanescent below this layer. Under TS conditions (wave frequency $f = \omega_0/2\pi$=48MHz, B_0=2.32T at antenna leading edge), the *R* cut-off layer for the main $n_{//}$=9 of a TS antenna with antisymmetric (dipole) strap phasing locates at the plasma density close to $n_e = 4.5\times10^{18}\mathrm{m}^{-3}$.

Equation 2 is solved over the whole simulation domain sketched in Figure 2. It features a 2D (radial/toroidal) cut into a straightened tokamak, where *x* is the toroidal direction, *y* is the radial direction, and the ignored direction *z* is the poloidal direction. Consistent with our 2D assumption, all derivatives with respect to *z* are assumed null. In this geometry the confinement magnetic field lies in the (*x*,*z*) plane and its pitch angle with respect to the toroidal direction is θ (see Figure 3). The cold plasma dielectric tensor 3 is rotated as the same convention as $\mathbf{B_0}$, and reads in the simulation coordinates

$$\boldsymbol{\varepsilon}_\mathbf{r}(\theta) = \begin{pmatrix} \varepsilon_\perp \sin^2\theta + \varepsilon_{//}\cos^2\theta & i\varepsilon_\times \sin\theta & -\varepsilon_\perp \sin\theta\cos\theta + \varepsilon_{//}\sin\theta\cos\theta \\ -i\varepsilon_\times \sin\theta & \varepsilon_\perp & i\varepsilon_\times \cos\theta \\ -\varepsilon_\perp \sin\theta\cos\theta + \varepsilon_{//}\sin\theta\cos\theta & -i\varepsilon_\times \cos\theta & \varepsilon_\perp \cos^2\theta + \varepsilon_{//}\sin^2\theta \end{pmatrix}_{x,y,z}$$

77* MERGEFORMAT ()

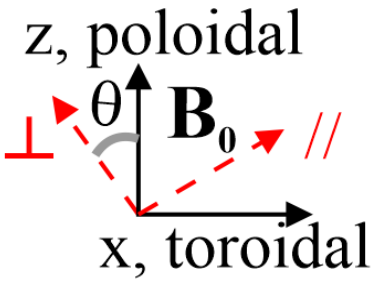

Figure 3. Tilted magnetic configuration in 2D SSWICH-Full Wave code

In Figure 2, the red dot rectangle marks the SOL region with open magnetic field lines. In this region, walls are shaped so that the incident angle of the magnetic field evolves gradually along the boundaries. This allows one to model the FW-SW mode conversion at those walls. The antenna has all the important components of a realistic Tore Supra antenna, i.e. side limiters, straps, septum and antenna box. They are treated as Perfect Electric Conductors (PEC) and thus are not meshed (see the blank elements). The antenna is assumed in vacuum so as to avoid the Lower Hybrid resonance as in [Lu 2016][Campos Pinto 2016].

To reproduce realistic wave radiation from antenna to the core, inhomogeneous plasma is implemented, where the magnetic field intensity and plasma density vary along radial direction *y*. Unlike some other codes [Louche 2015] based on CST microwave studio in which the plasma is divided into many slices of homogeneous plasma, SSWICH-Full wave uses directly the realistic density profiles measured in the experiments. In a real tokamak, this propagative FW heats the plasma core outside our simulation domain, *via* non-collisional processes that cannot easily be described within the cold plasma theory. To emulate full wave damping without reflection, a Perfectly Matched Layer (PML) technique is used: an equation similar to 2 is solved in a specific artificial dielectric and magnetic lossy medium introduced in [Jacquot2013] and generalized to tilted $\mathbf{B_0}$ in [Lu2016]. The

PML properties have been tuned to damp efficiently plane FWs with the main $n_{//}$ radiated by the antenna. To reliably describe the wave coupling, the radial PML was placed well beyond the R cut-off layer for the maximal $n_{//}$ in the radiated spectrum.

RF fields throughout the simulation volume are excited either by prescribing the RF current density at the surface of poloidal straps in the antenna box, or by prescribing the RF fields tangent to the antenna aperture (green boundary in Figure 2) from an external code. In this latter case both the poloidal and toroidal components are needed, whereas only $E_{//}$ contributed to the SW version. Both types of excitation will be used below, while only field map excitation was possible in the SW version.

COMSOL allows controlling the mesh size, to guaranty the required spatial resolution at minimal memory cost. Mesh is densest along the sheath boundary where the slow mode is expected, with 5×10^{-4}m element size, and sparsest inside the vacuum antenna (5cm size). In the SOL region, the mesh size is 1mm to be smaller than the typical slow wave evanescence length (~5mm). In the PML it is 3cm. All the mesh elements use triangular shape.

2.3 RF sheath BCs under tilted B_0

In the RF wave module, sheaths are implemented as Boundary Conditions (RF-SBCs) at the blue walls of Figure 2. In deriving RF-SBCs [D'Ippolito 2006], D'Ippolito assumes an electrostatic model for the oscillating sheaths, so that the RF electric field tangent to sheath/ plasma interface can be expressed as the gradient of an oscillating sheath voltage V_{RF}

$$E_t = -\nabla_t V_{RF} \qquad 88\backslash* \text{ MERGEFORMAT ()}$$

Where the subscript "t" denotes the two tangential components, i.e. the poloidal one and the one along the direction of the arc length of the curved wall. Combining Eq. 8 and the ansatz $\partial / \partial z = 0$, one gets $E_z = 0$ at our sheath boundaries. For vectorial wave equation 2, another scalar RF-SBC is needed and it comes from the sheath capacitance. [D'Ippolito 2006] gives the RF sheath boundary condition for a capacitive, "immobile ion" sheath

$$D_n = \frac{\varepsilon_{sh} V_{RF}}{\delta_{sh}(\alpha)} \qquad 99\backslash* \text{ MERGEFORMAT ()}$$

Where D_n is the electric displacement normal to the wall; ε_{sh} is the sheath dielectric permittivity; δ_{sh} is the Debye sheath width under tilted magnetic field, which can be derived according to the Chodura's magnetized sheath model [Chodura 1982][Stangeby 2012]. In this formula α is the incident angle of the magnetic field with respect to the wall, defined in our geometry as

$$\cos\alpha = \left|\mathbf{B_0}.\mathbf{n}\right| / B_0 = \left|n_x\right| \cos\theta \qquad 1010\backslash* \text{ MERGEFORMAT ()}$$

With $\mathbf{n}$ the unit vector locally normal to the wall. n_x is the x component of the normal direction of the curve. It is the local value calculated on each mesh point of the curve. $|n_x|$=1 on a flat boundary along y direction, and $|n_x|$=0 on a toroidal boundary. Eq. 9 analogizes sheath to a capacitor related to the charge separation that happens only inside the Debye sheath in the Chodura's model. We thus assume all the oscillating RF part is carried by the

Debye sheath, i.e. the Chodura's magnetic pre-sheath is time independent. Paper [Stangeby 2012] gives the potential drop at the Chodura's sheath,

$$V_{cs} = -\frac{k_B T_e}{e}\ln(\cos\alpha) \qquad 1111\backslash* \text{ MERGEFORMAT ()}$$

Where the subscript "*cs*" refers to Chodura's magnetic pre-sheath. Since the total voltage drop across the Chodura's sheath and Debye sheath is $V_{DC}+V_{RF}\cos(\omega_0 t)$, the voltage drop across the Debye sheath should be the following,

$$V_{DS}(t) = V_{DC} + \frac{k_B T_e}{e}\ln(\cos\alpha) + V_{RF}\cos\omega_0 t \qquad 1212\backslash* \text{ MERGEFORMAT ()}$$

Where the subscript "$_{DS}$" refers to the Debye sheath. Similar to the Child-Langmuir law [Child 1911][Langmuir 1913] for DC sheath, here we assume the Debye sheath width is a function of the DC part of $V_{DS}(t)$

$$\delta_{DS}(\alpha) = \lambda_{De}(\alpha)\left(\frac{eV_{DC}}{k_B T_e} + \ln(\cos\alpha)\right)^{3/4} \qquad 1313\backslash* \text{ MERGEFORMAT ()}$$

Where $\lambda_{De}(\alpha) = \lambda_{De}[\cos\alpha]^{-1/2}$ is the local Debye length at the edge of the Debye sheath, expressed as a function of the Debye length λ_{De} in the main plasma. The Debye length also depends on the incident angle since the density at the entrance of Debye sheath contains the incident angle. One can see when α=0°, Eq.13 falls back to the Child-Langmuir law[Child 1911][Langmuir 1913]. Eq. 13 fails to valid close to α=90°. In such an approximately parallel incident case, [Stangeby 2012] has proved that the Debye sheath disappears.

A more generalized form of the sheath RF impedance was proposed in [D'Ippolito 2015] recently. It releases the "immobile ion" assumption and both the resistive and capacitive part of the RF sheath are retained in their new model. At this stage, SSWICH-Full Wave code still uses Eq. 9 and thus the power dissipation in the volume of the sheath is not modelled. The two sheath boundary conditions $E_z = 0$ and Eq. 9 are implemented through the default Cartesian coordinates in COMSOL. In the RF field module, both $\delta_{sh}$and V_{RF} are assumed to be known from the other simulation modules, so that Eq. 9 is well defined. The PEC boundary condition is used at all the SOL boundaries parallel to $\mathbf{B_0}$.

2.4 RF Sheath oscillation module

The second simulation step in Figure 1 is to solve for V_{RF}. This quantity is only computed along sheath boundaries since it is only meaningful there. In our 2D model, V_{RF} is simply calculated *via* integration of E_t (the tangential component along the direction of the arc length) along the 1D curved sheath boundaries using Eq. 8. To determine the integration constant, V_{RF} is set to 0 at simulation points sitting furthest away from the wave launcher in the simulation domain.

2.5 DC plasma biasing module and DC sheath BCs under tilted B_0

The third step is to evaluate the DC plasma potential V_{DC} with respect to electrically grounded vessel walls. To save memory this quantity is only solved in the SOL region. The governing equation is the conservation of the DC current, assuming a phenomenological anisotropic Ohm's law is for the DC current transport. Here again the conductivity tensor used in [Jacquot 2014] is rotated under the same convention as the dielectric tensor.

$$\nabla\cdot(-\begin{bmatrix}\sigma_{//}\cos^2\theta+\sigma_{\perp}\sin^2\theta & 0\\ 0 & \sigma_{\perp}\end{bmatrix}\nabla V_{DC})=0 \qquad 1414\backslash^*$$

MERGEFORMAT ()

Where $\sigma_{//}$ and $\sigma_{\perp}$ are the parallel and perpendicular DC conductivities. $\sigma_{//}$ is estimated from the Spitzer conductivity [Spitzer 1953] which accounts for electron-ion friction. Under typical edge plasma temperature T_i=20eV, T_e=10eV, the Spitzer parallel conductivity is $\sigma_{//}=35714\ S/m$. $\sigma_{\perp}$ is less known and it is determined at this moment by matching the radial width of V_{DC} peaks with the experimental value as explained in [Jacquot 2014]. The transverse DC current at the edge plasma are most probably linked with the turbulent transverse transport. Work has been undergoing with SOL turbulence simulations to assess the perpendicular transport coefficients [Tamain 2016].

Three types of boundary conditions are associated with Eq. 14. We assume there is no perturbation to the main plasma, so V_{DC} at the separatrix equals to the floating potential without RF (V_f). Since we assume there is no sheath at //B_0 boundary, zero incident current (J_n=0) is assumed normal to these boundaries. Particle-in-cell simulations have shown the sheath rectification changes when the incident angle of the magnetic field evolves [Heuraux 2015]. A generalized sheath rectification formula was derived to account the tilted magnetic field at the sheath boundaries in a simple way. As the boundary is curved, the effective current density normal to the boundary is supposed to be the normal projection of the parallel current, which reads,

$$J_n=J_{is}^{\perp B}\cos\alpha\,(1-\min(\frac{J_{es}^{\perp B}}{J_{is}^{\perp B}},\exp(\frac{e(V_{\mathrm{f}}+V_b-V_{\mathrm{DC}})}{k_BT_e}))) \qquad 1515\backslash^*$$

MERGEFORMAT ()

Where the first term represents the ion conduction current, $J_{is}^{\perp B}$ is the ion saturation current. The second term is the electron conduction current, which is limited by $J_{es}^{\perp B}$. $J_{es}^{\perp B}$ is the electron saturation current. The superscript $\perp B$ represents the situation where the wall is perpendicular to $\mathbf{B_0}$. T_e is the electron temperature, k_B the Boltzmann constant. V_b is the extra biasing from V_{RF} computed in the second step. It is expressed as the modified Bessel function of the first kind I_0 [Jacquot 2012],

$$V_b=\ln I_0(V_{RF}) \qquad 1616\backslash^*\ \text{MERGEFORMAT ()}$$

Finally, the loop in Figure 1 is closed by applying Eq. 13 to update the sheath width.

2.6 Asymptotic first guess of solution.

One may note that the SBC Eq. 9 needs a prior knowledge of the sheath width, which is supposed to be estimated using the Eq. (12) after the computation of V_{DC}. To enter into the iterative loop, an asymptotic version was created under the wide sheath assumption [Colas 2012]. It assumes the sheath width goes to infinity and solves the three fields in segregated steps instead of using iterative scheme. Under this assumption, Eq. 9 reduces to D_n=0. At the transition points from the sheath boundaries to the metallic boundaries, a smooth function is added, which guarantees the sheath width has a continuous decay to zero. A typical run of the asymptotic version costs 6 mins, and the numerical convergence is generally well guaranteed. For Tore Supra runs with SW only [Jacquot2014], the results from asymptotic version were close to the final solution. All the numerical tests in this paper thus use only the asymptotic version.

2. INVESTIGATION OF THE ROLE OF THE FAST WAVE ON RF SHEATH EXCITATION IN TORE SUPRA CONFIGURATION WITH STRAP CURRENT EXCITATIONS

Until now, the SW was considered in most literatures as the main source term to generate RF sheath in the near-field region of the antenna. Using simulations close to the experimental conditions, in a TS case, this part aims at investigating how far the FW can contribute to RF sheath excitation which has already been seen in the DC current and potential maps. In this discussion several regions are traditionally distinguished:

- Material boundaries near field of the antenna, accessible to both FW and SW polarization radiated by the antenna.
- "Far-field" material boundaries, accessible to the FW only.

Since the DC plasma conductivity is very high along $\mathbf{B_0}$, it is also worth separating flux tubes magnetically connected to the antenna from unconnected field lines, and between them a buffer region where cross-field DC current transport might spread a bias [Jacquot2014].

To reproduce realistic FW propagation through the SOL, a realistic density profile from TS shot 40574 (red curve in Figure 4) is used. Magnetic tilt angle is θ=7° [Mendes 2010]. In this figure, as well as all the simulations provided in this section, we use a plasma composed of 95% D and 5% H, which is the typical compositions used in the hydrogen minority heating experiments [Jacquot 2013][Zhang 2015]. In addition, the following TS like parameters are taken: The magnetic field intensity B_0 scales as $1/R_a$, with R_a the major radius axis. B_0 at antenna aperture (y=0.224) is 2.32T, RF wave frequency f=48MHz. The excitation is done by imposing 1000A poloidal current with 180° phase difference on two straps. Figure 5 shows a typical poloidal RF wave field pattern (E_z) obtained in the simulation. The private SOL region is indicated by the black dot rectangle in Figure 5. It is the region bounded by two side limiters and the aperture. The rest SOL region is named as "free" SOL. Compared to Figure 2, here the curved top of the side limiters is slightly shifted upward in order to create a rectangular private SOL in the lower part that is consistent to the SSWICH-SW code.

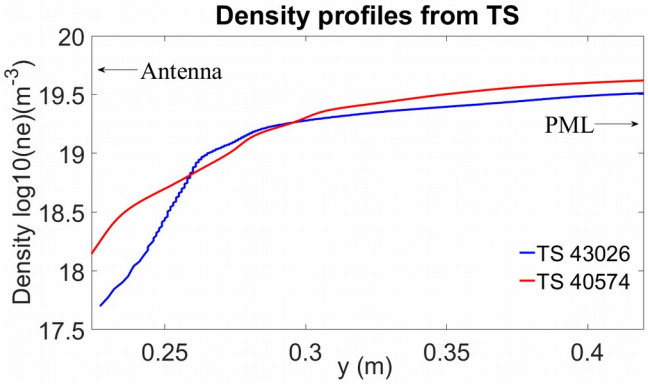

Figure 4. Density profiles used in this paper, data from Tore Supra shots 40574 and 43026, obtained by the reflectometry installed on Tore Supra

The *R* cut-off layer calculated from Eq. (10) of [Lu 2016] locates at y=0.248m (for the main lobe of the dipole phasing spectrum, $n_{//}$=9). As a reference, the antenna aperture lies at y=0.214m. The SW is evanescent almost everywhere in the simulation domain and in principle, it only appears in the private SOL and near shaped walls. The FW as well as the wave power propagates to the main plasma and then being damped in the PML, representing a full single-pass absorption in the real Tokamak experiment. The perpendicular wavelength of the FW in the main plasma is around 15cm, which is in agreement with the calculation by its dispersion relation Eq. 5. The toroidal power spectrum shown in *Figure 6* is calculated from the integration of the radial Poynting vector S_y along the radial PML/plasma interface. Its magnitude is normalized to satisfy continuous Parseval theorem. In this simulation, the main plasma toroidal width is extended to a large scale, 5m, in order to satisfy periodic conditions presumed by Fourier transformation. It seems the most efficient n_x or the center of main lobe does not change with different tilt angles. The power spectrum concentrates more on one direction when the tilt angle increases. The values of the tilt angle in *Figure 6* are chosen for the sake of completeness, although large tilt angles, i.e. θ=40° are clearly unrealistic in Tokamaks with large aspect ratios.

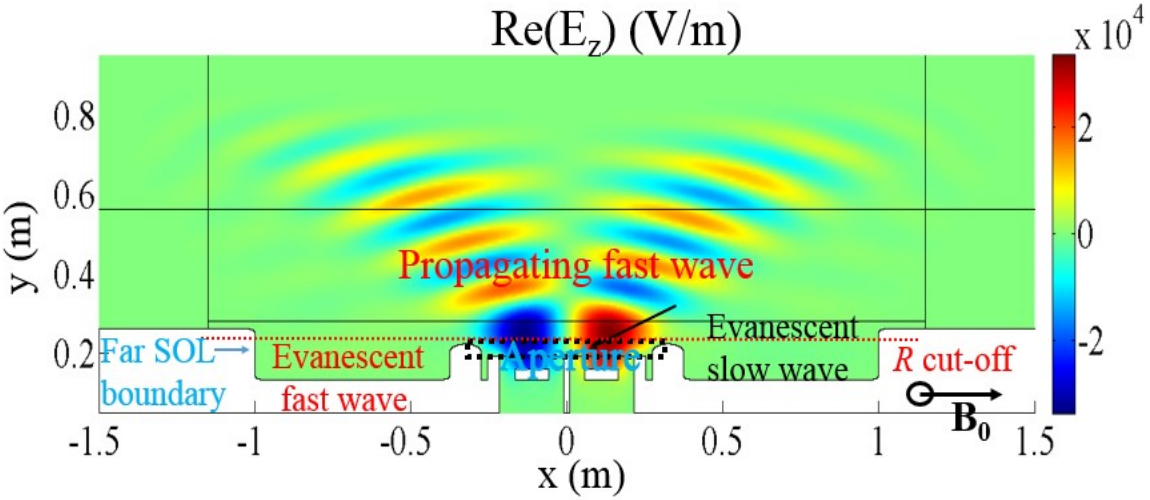

Figure 5.The real part of the poloidal electric field obtained by 2D SSWICH-Full Wave under Tore Supra configuration. The R cut-off layer of the FW for $n_{//}$=9 is shown by red dot line. The private SOL is enclosed by black dot rectangle. It is bounded by the limiters and the aperture. The antenna aperture lies at the bottom of the private SOL. Excitation by 1000A current on each strap with [0,π] toroidal phasing , magnetic field tilt angle 7°

To identify the role of the FW on RF sheath excitation in Tore Supra Tokamaks, three numerical tests are performed. The first test compares the parallel electric fields in the private SOL region obtained from the SSWICH-Full Wave and the SSWICH-SW simulations with the same input maps, to see the mode conversion between the FW and the SW. The second test aims at investigating the variation of the far field sheath properties and to check whether the sheath oscillation amplitude exhibits any kind of spatial proximity effect in the FW propagating region by tuning geometry dimensions. The final test compares the contribution of the FW on the V_{DC} radial broadening with the DC current transport mechanism by artificially changing the perpendicular conductivities and the cold plasma dielectric tensor.

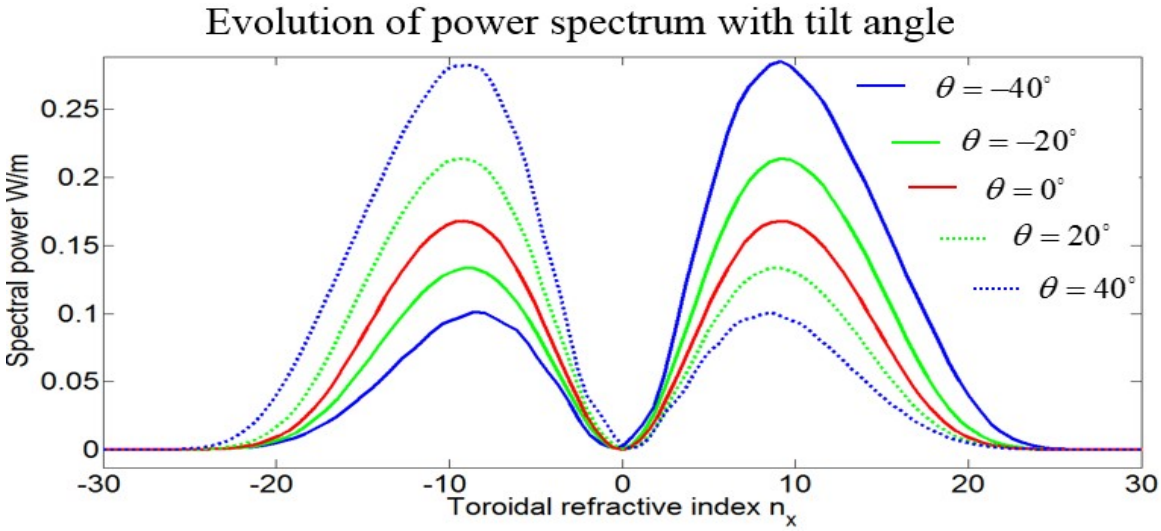

Figure 6. Toroidal power spectrum under different tilt angles. Data were extracted at the radial PML/plasma interface

3.1. FW→ SW mode conversion upon reflection at tilted wall

The 2D SSWICH-Full Wave code solves simultaneously the FW and the SW polarizations, whereas the 2D SSWICH-SW code only deals with the evanescent SW. By comparing the SW component of SSWICH-Full Wave simulation with those of SSWICH-SW simulations under the same conditions, one can immediately find out the impact of the FW. In this test, we removed all the curved geometry in the SSWICH-Full Wave code in order to match the flat geometry of the SSWICH-SW code. A constant density ($=1.5\times10^{18}m^{-3}$) is imposed all through the private SOL region. In this region, both of the FW and the SW are evanescent. The SW has an evanescence length around 3mm by Eq. 6. The magnetic tilt angle in the SSWICH-Full Wave code is set to θ=0.01° to approach θ=0°, corresponding to the tilt angle in the SSWICH-SW code. The $E_{//}$ field map at the aperture of the SSWICH-Full Wave is used as an input field map to the SW code. We then compared the electric field pattern in the private SOL region. The results are shown in Figure 7. The left and the right figures show the results from the SW simulation and the full wave simulation, respectively. In the right figure, a large $E_{//}$ pattern appears at the top corners of the side limiters, which does not exist in the left figure. The SW is evanescent before reaching those points, thus we expect it is the FW that propagated to that position and then mode converted to the SW. The field pattern does not change when finer meshes are used. This observation is similar to the simulations reported in [Kohno 2015], where mode conversion to the SW occurs when the wall geometry exhibits a sharp transition.

Further tests are done to justify our speculation. We compared the evolution of $E_{//}$ under an artificial change of $\varepsilon_{//}$. Since the evanescence length of the SW Eq. 6 is inversely proportional to $\sqrt{|\varepsilon_{//}|}$, reducing $\varepsilon_{//}$ by a factor of 10, the SW evanescence length should be almost 3 times' larger and hence the wave can propagate further radically. On the other hand, the FW dispersion relation is independent on $\varepsilon_{//}$ but sensitive to the change of $\varepsilon_{\times}$. Reducing $\varepsilon_{\times}$ can make the FW more evanescent, whereas $\varepsilon_{\times}$ has no significant impact on the SW. Reducing $\varepsilon_{\times}$ by a factor of 10, the field structure could be significantly reduced, however the SW evanescence length should not be affected. All those points are confirmed by the dedicated simulations not shown here. Another test is to change the magnetic tilt angle in the full wave code to see its impact on mode conversion and on the generation of asymmetry. When the magnetic field is increased from 0° to 20°, Figure 8 shows that $E_{//}$ pattern still roughly keeps the left-right symmetry at the lower part of the private SOL region where the SW field is dominant. However the symmetric check shows the quantity $E_{\perp}(x)+E_{\perp}(-x)$ changes from 0 V/m to 3 V/m. In other words, the anti-symmetry of $E_{\perp}$ is lost when $\theta=20^{o}$. We also saw in Figure 8 that the $E_{//}$ at the left top of the limiter increases, while decreases at the right top. This opposite variation matches the variation of $E_{\perp}$ and it also coincides with the FW spectrum variation w.r.t the tilt angle, i.e. Figure 6. The last observation again suggests the field pattern at the top of the limiters is indeed associated with the FW mode conversion.

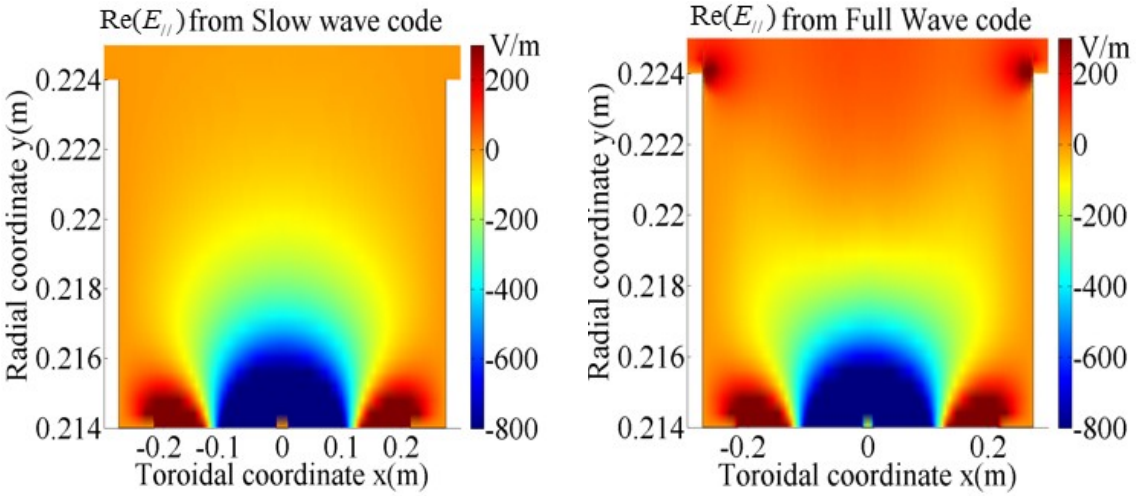

Figure 7. Left: $E_{//}$ obtained from SSWICH-SW code; Right: $E_{//}$ obtained from SSWICH-Full Wave code, $\theta=0^{o}$

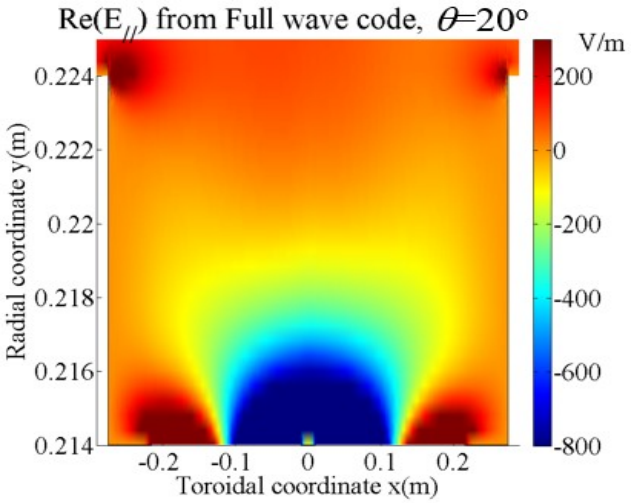

Figure 8. $E_{//}$ from SSWICH-Full wave code with larger magnetic tilt angle

A direct comparison of the SSWICH-Full Wave and the SSWICH-SW simulations have shown above that the mode conversion from FW to SW occurring at the sharp corners where the boundary shape varies rapidly. Indeed, based on the fact that the SW and the FW have different behaviours when the Stix component evolves and its opposite variations w.r.t the tilt angle, we found that the field pattern appears at the leading edge of the side limiter is more likely a mode converted SW.

3.2. FW induced far field RF sheath & FW proximity effects in its propagating region

At the Tokamak edge, the FW can propagate much further away from the wave launcher than the evanescent SW and thus it can in principle excite sheath in remote areas. The FW induced far field RF sheath has been observed intensively by Alcator C-mod observations [Ochoukov 2014]. In the following SSWICH-Full wave simulation, we monitored the sheath RF oscillations far away from the antenna. A constant density profile higher than the FW *R* cut-off density was imposed in the free SOL region, so that the FW is propagative in the free SOL region and it can reach the upper-left boundary (purple circle in Figure 2). The magnetic tilt angle is set to 1°. The wall curvature is kept in the SOL region, as it is in Figure 5. Mode conversion is still present at the rounded corners even when $\theta = 0^{o}$as the magnetic field is neither perpendicular nor parallel to the curved boundary. V_{RF} is excited preferentially near these rounded corners. This justifies why the intense V_{RF} is observed when the geometry changes rapidly [D'Ippolito 2013]. In the previous simulation performed by 2D SSWICH-SW code, V_{RF} at this boundary was very low. By contrast our full-wave simulations managed to excite significant $|V_{RF}|$ at this far field boundary, exceeding 100V for some cases. This is a first indication of a role for the FW at these locations.

In Figure 2, we have defined two characteristic dimensional lengths, the toroidal and the radial length of the free SOL region, $L_{//}$ and $L_{\perp}$, respectively. By tuning the $L_{//}$ and $L_{\perp}$ (change of $L_{\perp}$ is done by shifting downwards the antenna structure with respect to the separatrix), one could see the impact of these lengths on the excited far field RF sheath at the upper-left sheath boundary. By lack of computer memory these numerical tests used $L_{//}$ values smaller than the experimental ones (more than 10m in [Kubic2013]). The $|V_{RF}|$ variations over the scans of $L_{//}$ and $L_{\perp}$ are shown in Figure 9 and Figure 10. $|V_{RF}|$ at that boundary decreases under larger toroidal dimensions, and becomes small as $L_{//}$ reaches 3m.

$|V_{RF}|$ increases with larger $L_{\perp}$, which is counter-intuitive at first sight: RF sheath excitation gets more intense as the extremity of the wall moves farther from the antenna. It is against the prediction by the spatial proximity effect to the wave emitters, which was proposed to explain the experimental RF sheath properties due to the evanescent SW [Colas 2017]. To explain why the distance between the wave launcher and the target sheath boundary does not really matter here, we propose to invoke the FW propagation properties. By this interpretation, sheath excitation might depend on the distance between the FW propagation cone (exhibited in *Figure 5*) and the target sheath boundary. Increasing $L_{\perp}$ actually decreases the distance between the upper-left boundary and the FW propagation cone. This is a second indication of a role for the FW. This observation suggests that the spatial proximity effect, if any is at play, needs to be defined differently in the various regions with various wave behaviours. Spatial proximity effects in the near field zone will be examined below in section 4.2.

By tuning the toroidal and radial dimensions of the SOL region, we have observed above the RF sheath oscillations appearing at the shaped walls far away from the antenna. The evolution of the $|V_{RF}|$ w.r.t the dimension lengths is interpreted by the properties of the FW propagation, which suggests that the FW plays a dominant role on the RF sheath excitation in the far SOL region.

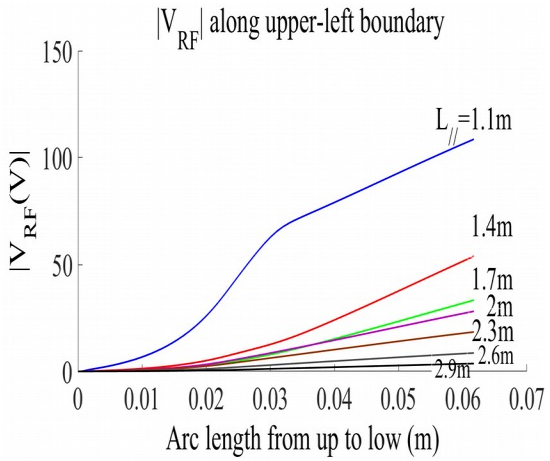

Figure 9. $|V_{RF}|$ at the upper-left sheath boundary of Figure 2 varies with a scan of $L_{//}$, $L_{\perp}$=0.0375m

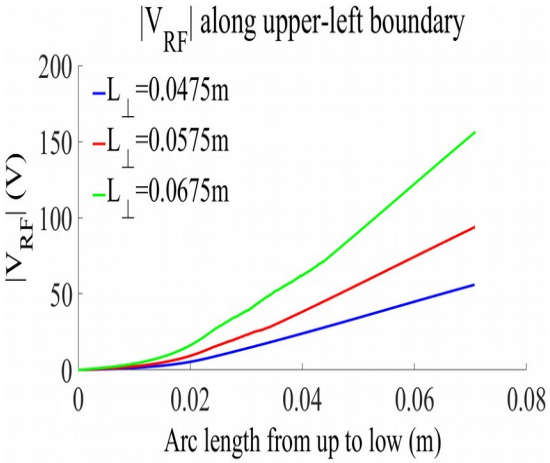

Figure 10. Variation of $|V_{RF}|$ at the upper-left sheath boundary of Figure 2 with a can of $L_{\perp}$, $L_{//}$=2m, other conditions are the same as Figure 9

3.3. DC current transport vs. FW contribution on radial width of V_{DC} peak in free SOL

A typical V_{DC} structure excited by the 2D SSWICH-Full Wave code is shown in Figure 11 (a). The magnetic tilt angle in this figure is 7°, which is the typical value found on Tore Supra. V_{DC} is most intense at the private SOL since both the SW and the FW are present there. Although the SW only appears in the private SOL, the V_{DC} structure can extend further away radially and toroidally, via the transport of DC currents. This is one way to explain why the RFA locating 12m away from the wave launcher in [Kubic 2013] can still record significant modifications of the SOL. The radial extension of the V_{DC} peak in the free SOL (shown by the blue double-headed arrow on both sides of the antenna limiter tip) was explained previously in the 2D SSWICH-SW code by DC current transport mechanism, for which two ad-hoc conductivities$\sigma_{\perp,p}$,$\sigma_{\perp,f}$ are introduced to distinguish different turbulence levels between the private SOL and the rest SOL region, i.e. free SOL. Those conductivity

values are unfortunately badly known. Nevertheless, a domain of these values has been determined by matching the simulation with experimental radial broadening of V_{DC} [Jacquot 2014]. The two conductivities used in Figure 11 (a), $\sigma_{\perp,f} = 7.1\times10^{-8}\sigma_{//}$, $\sigma_{\perp,p} = 2.6\times10^{-6}\sigma_{//}$ are taken within this domain[Jacquot 2014]. The V_{DC} radial width under these perpendicular conductivities is around 2 cm, similar to that obtained from the RFA measurement on Tore Supra [Kubic 2013]. Suppression of these two perpendicular conductivities will simultaneously reduce the DC current transport. One can see thereafter if the FW solely could produce a SOL biasing by exciting RF sheaths on the walls far from the antenna. In addition, the FW is sensitive to the change of the off-diagonal term of the Stix tensor: $\varepsilon_{\times}$. Thus the FW contribution to the V_{DC} should be affected by reducing $\varepsilon_{\times}$. Along these reasoning, we further plotted the V_{DC} map with reduced perpendicular conductivity and reduced $\varepsilon_{\times}$, respectively. The results are shown in Figure 11(b) and Figure 12.

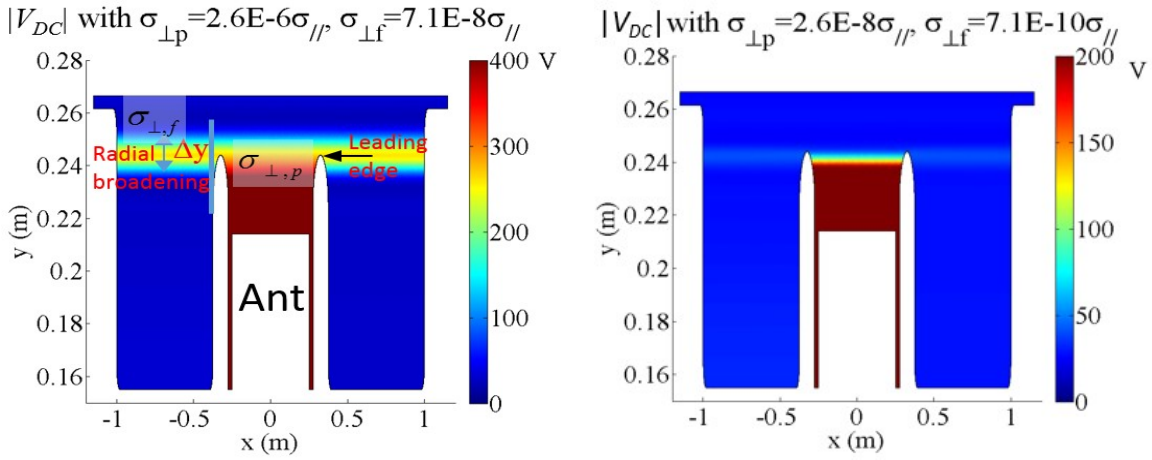

Figure 11. (a) V_{DC} flux solved in the SOL region (red dot rectangle in Figure 2), plasma temperature T_i=20eV, T_e=10eV. V_{DC} radial broadening Δy is marked by the blue double-headed arrow. The black arrow indicates the leading edge of the right side limiter. The blue radial line shows where the data are extracted in Figure 14-Figure 16. (b) $|V_{DC}|$ after reducing the perpendicular conductivity by 100 times, other parameters are the same as (a)

Comparing Figure 11 (a) with Figure 11 (b), we see that decreasing the perpendicular conductivity can significantly affect the V_{DC} radial broadening even in the presence of the FW. $|V_{DC}|$ is higher with a larger $\sigma_{\perp,p}$ at the leading edge of the limiters (its location is shown by the black arrow in Figure 11 (a)). This can be understood naively that with a larger $\sigma_{\perp,p}$, ∇V_{DC} is smaller to fulfil Eq. 14. Thus the transversal diffusion length, expressed by Eq. (1) in [Jacquot 2014], is larger in the private SOL or V_{DC} decreases slower radially starting from the aperture. Given V_{DC} at the aperture, V_{DC} at the leading edge of the limiters is consequently larger.

Comparing Figure 12 with Figure 11 (a), one can see that the radial broadening only varies slightly with different $\varepsilon_{\times}$. These observations together suggest that in the present simulations, the DC current transport described by the perpendicular conductivity is still the dominant mechanism to explain the free SOL biasing.

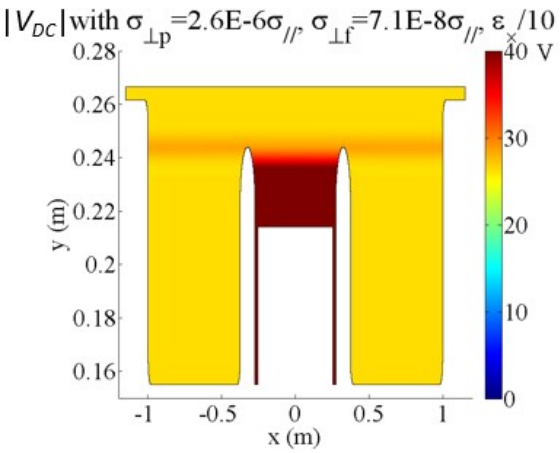

Figure 12. $|V_{DC}|$ after tuning the off-diagonal term of Stix tensor under the same plasma conditions as Figure 11

To summarize this section, asymptotic 2D SSWICH full-wave simulations with TS-like parameters evidenced FW contributions to RF sheath excitation: mode conversion upon wave reflection and excitation of far field sheaths in the main SOL far from the active antenna. Yet these processes cannot explain why the V_{DC} peaks measured on TS are centred radially near the leading edge of the antenna limiters magnetically connected to the diagnostic. They can neither reproduce the radial extension of these peaks.

3. 2D SSWICH-FULL WAVE SIMULATIONS WITH REALISTIC INPUT FIELD MAPS FROM 3D RAPLICASOL JOINT SIMULATIONS

Up to here, the results we discussed above were obtained using the current excitation by imposing poloidal currents on the build-in antennas. When comparing the simulation with the experiment, it is better to use a more realistic excitation. Moreover, SSWICH-Full Wave is limited in 2D at this moment. In order to compare with the 3D experimental results, one has to use a multiple-2D approach, i.e. exciting several independent 2D simulations with full-wave field maps from the 3D RAPLICASOL code [Jacquot 2015] at different z (poloidal) altitudes. This section tries to recover the double-hump structure in Figure 6a of [Corre 2012] and the left-right asymmetry of the differential temperature map in Figure 5 of [Colas 2013], by joint simulations using 2D SSWICH-Full wave and 3D RAPLICASOL.

The realistic antenna has a poloidal curvature to match the shape of the vacuum vessel, thus the poloidal direction is not exactly vertical. For simplicity, this curvature is not considered in our simulation. For SSWICH-SW, the multiple-2D approach is shown to be a fairly good approximation of the realistic 3D simulations [Colas 2017]. A similar assessment was made below for the FW.

The 3D RAPLICASOL code models a realistic Tore Supra antenna geometry including a Cantilevered Bars and Slotted Box (CBSB) Faraday screen, as modelled in [Jacquot 2014]. The RF fields in RAPLICASOL are computed using the following Tore Supra parameters: $\mathbf{B_0}$ at aperture (y=0.214m)=2.9T, RF wave frequency 57MHz, θ=7°. The radial extension of the private SOL is 1cm as in the real Tore Supra, i.e. the leading edge of the side limiter locates at y=0.224m, as shown in Figure 2. The other parameters are the same as used in Figure 5. A realistic density profile from Tore Supra shot 43026 (blue curve in Figure 4) is used. Under this density, the SW radial evanescence length is about 1cm (value at y=0.224m, $n_{//}$=10). The FW R cut-off layer locates at y=0.244m ($n_{//}$=10), thus the FW is evanescent in the private SOL. The simulation in 3D RAPLICASOL is done with PEC BCs only. It is further normalized to 1MW total coupled power.

In the first approximation for large $|\varepsilon_{//}|$, the FW is a Transverse Electric (TE) mode while the SW is a Transverse Magnetic (TM) mode. Here the transverse means perpendicular with respect to the direction of the $\mathbf{B_0}$. For k_z=0 this also means that the poloidal electric field is negligible in the polarization of the SW. These distinct features allow one separating the FW and the SW on RF excitation. The $E_{//}$ and $E_{\perp}$ map are extracted at the Faraday screen of the 3D RAPLICASOL. These field maps are shown in *Figure 13*. The $E_{//}$ map shows a clear double-hump structure at the lateral edges of the side limiters and at the end of the FS bars, whereas the $E_{\perp}$ has only a single hump and spreads over a large scale. The $E_{//}$ is significantly smaller than the $E_{\perp}$ at the FS bars, which is normal since the FS is used for cancelling the $E_{//}$ from the excitation. These field maps are decomposed into the toroidal and vertical components and then imported at the aperture of the 2D SSWICH-Full Wave code.

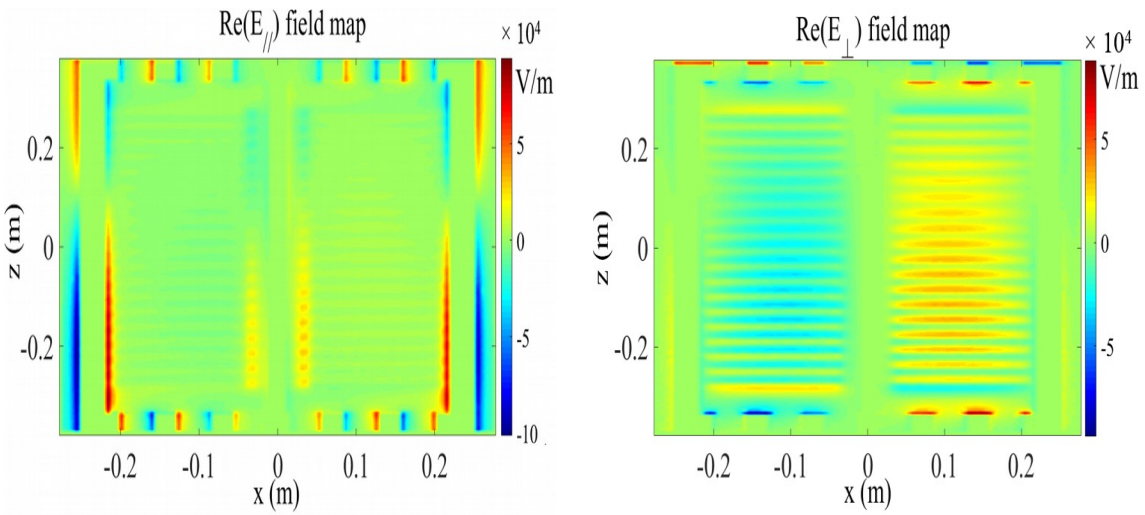

Figure 13. 2D field maps generated at the Faraday screen of the 3D RAPLICASOL code with 1MW power injected; Left: the real part of the parallel component; Right: the real part of the perpendicular component (vertical component).

2D SSWICH-Full Wave simulations are carried out with the same plasma parameters and density profile as RAPLICASOL runs. We chose the parallel connection as large as possible using our dedicated workstation with 128 GB of memory, i.e. $L_{//}$ =4.7m. The perpendicular DC plasma conductivity $\sigma_{\perp,f} = 10^{-8}\sigma_{//}$ is used in the free SOL to match the radial extension of the V_{DC} in free SOL. A scan of the vertical position from z=-0.376m to 0.378m (bounded by the vertical length of the FS) with a step size of 3mm is done. For each vertical position, 2D SSWICH-Full Wave code was run once with the input electric field map from 3D RAPLICASOL at that vertical position and then the V_{DC} data at the left edge of the left limiter (shown by the blue radial line in *Figure 11*(a)) was extracted.

4.1. V_{DC} poloidal structure

The first set of simulations excites SSWICH-Full Wave with only the $E_{//}$ component of the RAPLICASOL field map, representing a V_{DC} produced uniquely by the SW excitation. The result (Figure 14) recovers the double-hump shape observed by the RFA measurement and previous SSWICH-SW runs [Jacquot 2014]. It is plotted in radial/vertical plane at the toroidal position of the blue radial line in *Figure 11*(a). The abscissa is centered at the radial position of the leading edge of the side limiter, i.e. y=0.224 in Figure 2. With our choice of

transverse DC conductivity and $L_{//}$, the radial broadening of V_{DC} is about 3cm, which is consistent with the measurement although the parallel connection length in our simulation is smaller than those in Tore Supra free SOL by at least a factor of 2. The double-hump structure however vanishes when only the $E_{\perp}$ is imposed at the aperture, representing the dominant FW excitation (see *Figure 15*). *Figure 16* shows the V_{DC} distribution over a vertical scan with full (both $E_{//}$ and $E_{\perp}$) excitation at the aperture. Unlike V_{RF} in our asymptotic simulations, the "total" V_{DC} in presence of $E_{//}$ and $E_{\perp}$ field map excitation is not a simple addition of the two individual contributions from the FW and the SW since the sheath rectification process Eq.15 is non-linear. The scale of V_{DC} in Figure 15-Figure 16 is comparable with the experimental value (~100 volts), but not really the poloidal shape.

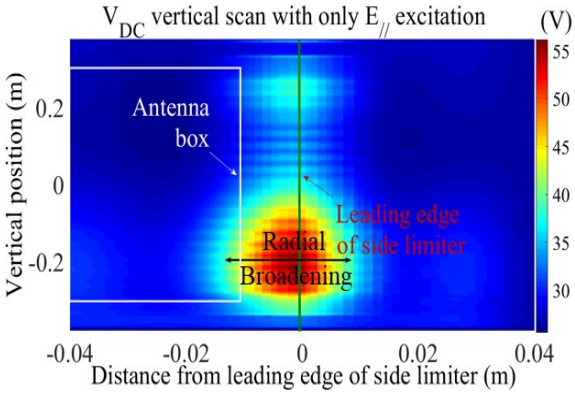

Figure 14. V_{DC} vertical scan using multiple-2D approach with only $E_{//}$ map used at the aperture. The double-headed arrow indicates the radial broadening of V_{DC}. In each vertical position, data are picked up at the blue line of Figure 11 (a)

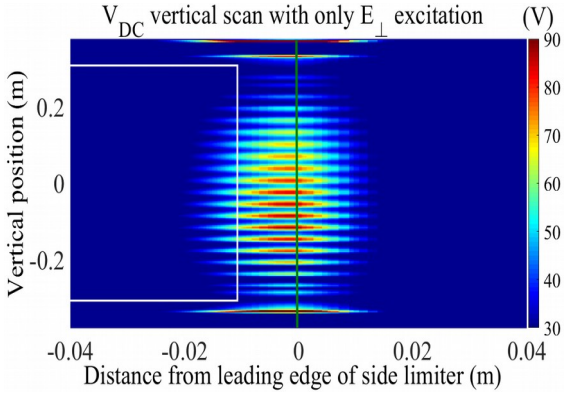

Figure 15. V_{DC} vertical scan with only $E_{\perp}$ electric field map imposed at the aperture The white rectangle shows the boundary of the antenna box. Green line shows the location of the leading edge of the side limiter.

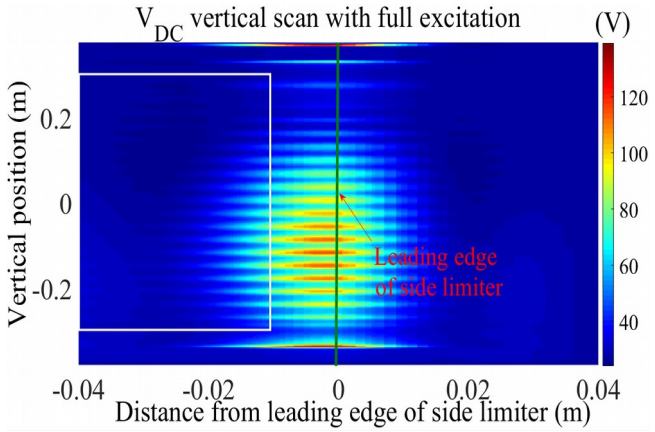

Figure 16. V_{DC} vertical scan with the full electric field map imposed at the aperture under the same plasma conditions used in Figure 14 and Figure 15

The vertical modulation of V_{DC} in *Figure 15* is caused by the Faraday screen bars in the RAPLICASOL code. It can also be seen in the $E_{\perp}$ field map (Figure 13 Right). However such poloidal modulation is not obvious in the experimental measurements, although its typical period (~3cm) is within the spatial resolution of infrared cameras (the FS bars are clearly visible on the IR pictures). One might look for artefacts in the measurements. Here we rather re-assess for the FW the multi-2D approach successfully applied for the SW simulations, looking for a possible over-estimation of the poloidal modulation compared to full-3D calculations.

A typical scale of perpendicular wave number of the FW and the SW at the blue line of *Figure 11*(a) can be evaluated from their dispersion relations Eq. 5 and Eq. 4, i.e. $k_{\perp,fw}^2 = -100\,m^{-2}, k_{\perp,sw}^2 = -10^5\,m^{-2}$. The squared radial wavenumber reads: $k_y^2 = k_\perp^2 - k_z^2$. Our multi-2D approach amounts to taking k_z=0 m^{-1} for all spectral components in the input field map, whereas in real 3D calculations, a finite k_z should be present, whose magnitude ($2\pi/0.03$~200m^{-1} for 3cm modulations) is larger than the ¿$k_{\perp,fw}$∨, while being much less than the ¿$k_{\perp,sw}$∨¿. Thus the FW can be more sensitive than the SW to a finite k_z. Adding a finite k_z will make k_y^2 more negative and increases the radial evanescence of the FW. Correspondingly, the local field modulation will become less intense. Thus the amplitude of V_{DC} modulation shown in Figure 15 is probably overestimated. A crude way to mitigate the poloidal modulation is to smooth the $E_{\square}$ field map. In the following simulation, we average $E_{\square}$ over a period of 3cm in the poloidal direction. This can eliminate the fast modulations which has k_z □200m^{-1}. The V_{DC} scale indeed decreases by 30%. The correct way to model preciously the FW contribution on V_{DC} poloidal structure is to take into account all the k_z. At this moment, a full 3D simulation is out of reach, both by lack of appropriate formulation for the SBCs and due to the excessive memory requirements. Work is undergoing to incorporate some 3D effects (i.e. k_z spectrum) by treating the poloidal direction in the spectral domain. The results shown in Figure 15 and Figure 16 could possibly get improved in the future.

4.2. Left-right heat flux imbalance

The final numerical simulation aims at recovering the left-right asymmetry observed from the differential surface temperature map in [Colas 2013]. Neglecting the transverse heat exchanges in the materials, the temperature measurement in thermal steady-state is a direct indication of the heat flux normal to the antenna surface. Thus we will examine whether the heat flux in our simulation exhibits left-right asymmetry in case of unbalanced strap feeding. In the 3D RAPLICASOL code, it is feasible to change the power ratio over the two straps still phase [0, π]. Two maps of the RF field components tangent to the Faraday Screen were used as input, with power ratio of respectively 50%-50% and 63%-37%. The next step is to calculate the heat flux at the lateral sheath boundary of the private SOL, i.e. the boundaries enclosed by red ellipses in Figure 2. The effective heat flux is the one normal to the boundary, which can be determined via the following analytical expression,

$$Q_n = j_{is}^{\perp B}[V_{DC}(x,y) + 2.5\frac{k_B T_i}{e}]\cos\alpha + \frac{2k_B T_e}{e} j_{is}^{\perp B} \min\{\frac{j_{es}^{\perp B}}{j_{is}^{\perp B}}, \exp[e\frac{V_f + V_b(x,y) - V_{DC}(x,y)}{k_B T_e}]\}\cos\alpha \qquad 1717\backslash*$$

MERGEFORMAT ()

Where the first term is the averaged ion heat flux [Stangeby 2000] averaged over one RF cycle; the second term corresponds to the time-averaged electron heat flux. It is a simple estimation valid for the thermal electrons and each electron hitting the wall carries an average energy $2k_B T_e/e$ [Stangeby 2000]. Eq. 17 is a generalized form which treats the impact of the tilted $\mathbf{B_0}$ and curvature in a simple way.

By Eq. 17, the heat flux at the two lateral boundary of the private SOL at z=-0.2m was evaluated. The results are shown in *Figure 17*. The left-right asymmetry was nicely recovered. This left-right asymmetry is a robust invariant property that appears at all vertical positions. The origin of this asymmetry comes from the tilted $\mathbf{B_0}$ and the unbalanced power ratio at two straps. This suggests that in sheath excitation by full-wave

fields, the spatial proximity effect between launching structures and the observed walls still matters in the region where the evanescent SW and evanescent FW co-exist.

In the private SOL with short connection lengths, due to the large DC parallel conductivity of the plasma, V_{DC} is nearly homogeneous along the open magnetic field lines and is almost the same at its both extremities (see Figure 11-Figure 12), despite V_{RF} being different at the left and right sides. Consequently the left-right heat load asymmetry cannot arise from ion heat fluxes, depending on V_{DC} only. Nevertheless, V_b are different at the left and right boundaries. Therefore the heat load asymmetry arises from a larger amount of electrons hitting the wall with larger V_b. This stresses the need, in order to reproduce the asymmetry, to drop the floating sheath boundary conditions and allow DC current exchanges between several parts of the wall. In *Figure 17* close to the aperture, the sheath rectification is so strong that the electron current gets saturated to a value independent of V_b. At this stage, the electron saturation current only depends on plasma parameter while it is invariant to the power ratio at straps. Then as one moves towards the top of the limiter, sheath rectification become moderate so the electron heat flux and thus the total heat flux is correlated with the RF field and thus the power ratio. The sharp drop of the electron flux at the two figures does not occur at the same radial position. This is because the electron current depends on the biased potential V_b and thus the local RF electric fields. Under a tilted magnetic field, the local wave pattern is not exactly left-right symmetric, as we have seen in the power spectrum (Figure 6). Therefore a small amount of asymmetry still remains even with balanced strap feeding. After a certain point, the sheath rectification is so low that the electron heat load is negligible compared to the ion heat flux. The ion heat flux depends on the V_{DC}. But it is not very sensitive to a small change of the power balance. In the simulation, V_{DC} amplitude only changes by 4% with these two power ratios. At the leading edge of the limiter, heat flux becomes zero as the boundary is parallel to $\mathbf{B_0}$.

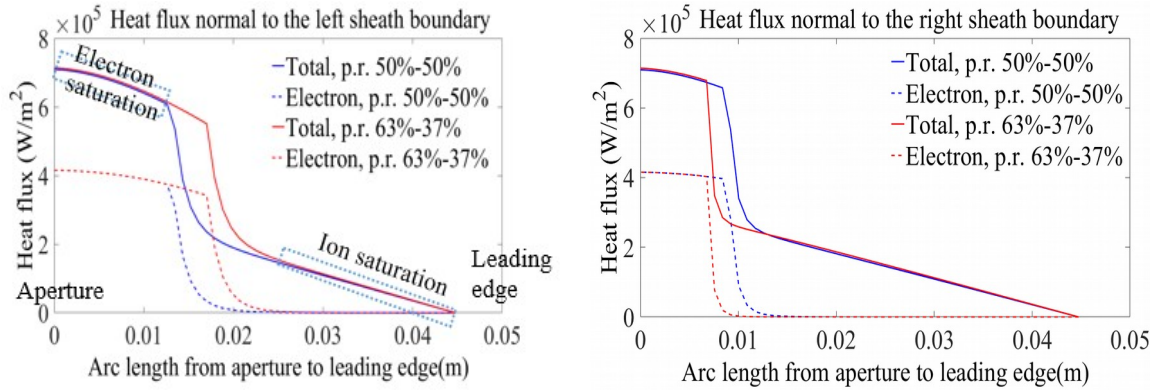

(a) *(b)*

Figure 17. Heat flux evaluated by Eq. 17 at the curved boundaries enclosed by red ellipses in Figure 2 for 1MW power coupled to the plasma. Magnetic tilt angle¿ 7°, Data are picked up at the vertical altitude z=-0.2m. (a) Heat flux at the left sheath boundary; (b) Heat flux at the right sheath boundary. The solid curves are the total heat flux, while the dashed curves counts only the electron heat flux. The blue curves use a balanced power ratio of 50%-50%, whereas the red curves have a unbalance power ratio of 63%-37%

4. CONCLUSION AND PROSPECTS

This paper presented a new version of the SSWICH code to model RF sheaths over the size of a realistic ion cyclotron antenna in a tokamak. The upgrades that we have developed and tested include the fast wave (FW) and the slow wave (SW), a realistic magnetic field configuration and shaped walls. At this stage, the electrical properties of magnetized RF

sheaths presently incorporated in the sheath BCs remain simple. Some improvement is needed in this front.

Asymptotic SSWICH-Full Wave simulations of typical tokamak experiments have shown the mode conversion of FW into SW occurring at the sharp corners where the boundary shape varies rapidly. It has also evidenced "far-field" sheath oscillations appearing at the shaped walls with relatively long magnetic connections to the antenna. Due to the limited computational resources the simulated connection lengths are still smaller than real ones. By tuning the toroidal and radial dimensions of the wall boundaries in the FW propagation region, we evidenced enhanced $|V_{RF}|$ with larger radial distance of the sheath walls to the wave-launching structure. This suggests that "spatial proximity effects", as introduced in [Colas2017], are irrelevant for the propagating FW and need to be redefined. A possible alternative could involve the proximity to the FW propagation cone emerging from the antenna. Simulated $|V_{RF}|$ amplitudes at the shaped far SOL boundary indeed decrease with larger distance to this cone. This behaviour correlates again the sheath oscillations can with the propagating FW.

In the "near field" regions where both the FW and the SW are evanescent, we re-evaluated with SSWICH-Full Wave the heat flux along two toroidally opposite antenna side limiters. Simulations could reproduce qualitatively the left-right heat load asymmetry that has been observed extensively in the strap power unbalance experiments. This suggests that, under full wave polarizations, the previous definition of the "spatial proximity effects" is still relevant in the vicinity of the wave launcher.

Even the in presence of propagating Fast Waves, the DC current transport was still found as a necessary mechanism to reproduce in our simulations the radial width of V_{DC} peaks observed experimentally. SSWICH-FW therefore does not remove the inherent uncertainties in quantitative calculations of DC potentials, already mentioned in [Jacquot2014], due to a poor knowledge of the DC current transport mechanisms. Yet, once DC conductivities are fixed, relative comparisons of sheath voltages are still possible, in particular for antenna design assessment.

While most of the FW-related effects expected in 2D were observed in our simulations, 3D effects seem to be important to estimate the FW contribution on the V_{DC} poloidal structure. SSWICH-Full Wave / RAPLICASOL joint simulations have recovered the double-hump poloidal structure measured in the experimental surface temperature and potential maps. But the simulation matches better with this experimental structure when only the SW excitation is accounted for. The need for 3D effects was identified for correctly propagating FW with small characteristic poloidal lengths (e.g. RF field modulations by FS bars). While a full-3D version of SSWICH seems presently out of reach with our computational resources, work is ongoing to incorporate the finite poloidal wavenumbers in 2D simulation using a spectral treatment in the poloidal direction.

Our final goal with SSWICH code is to implement a 3D realistic geometry, a full wave treatment and 3D sheath boundary conditions. The 3D RAPLICASOL code solving full wave propagation without sheaths is now available. It will replace the current RF module in the 3D version of SSWICH-Full Wave code when the 3D SBCs are available. In the future, SSWICH can work together with other codes, for example, the EMC3-Eirene code [Zhang 2016] to cover the RF induced density modification and gas puffing.

Testing different kinds of antennas and plasma types under the framework of an international cooperation helps to put constraints on the models. The role of the FW identified numerically in this paper can be examined experimentally using B-dot probes [Ochoukov 2014]. By comparing the FW component of the B-dot probe signal with the

strength of the measured plasma potential, one can find the correlation between these two quantities and then check which wave is dominant on RF sheath rectification both in the vicinity of wave launcher and at the far SOL boundaries.

ACKNOWLEDGMENTS

This work has been carried out within the framework of the EUROfusion Consortium and has received funding from the Erasmus Fusion-DC and the Euratom research and training programme 2014-2018 under grant agreement No 633053. It is a part of enabling research project WP15-ER-01/CEA-05. The views and opinions expressed herein do not necessarily reflect those of the European Commission.

REFERENCE

1. [Bobkov2015]: V. Bobkov et al., AIP Conf. Proc. 1689, 030004-1 030004-8 (2015)
2. [Bobkov 2017] V. Bobkov *et al*, , *Plas. Phys. Cont. Fusion*, **59** (2017) 014022
3. [Child 1911] C. D. Child, "Discharge from hot CaO", *Phys. Rev*. (Series I), **32** (1911) 492
4. [Campos Pinto 2016] M. Campos Pinto and B. Despres, "Constructive formulations of resonant Maxwell's equations", hal-01278860
5. [Chodura 1982] R. Chodura, "Plasma-wall transition in an oblique magnetic field", *Phys. Fluids*, **25** (1982) 1628
6. [Colas 2009] L. Colas *et al*. "Ion cyclotron resonant heating in Tore Supra", *Fus. Sci. Tech*., **56** (2009) 1173-1204
7. [Colas 2012] L. Colas, J. Jacquot, S. Heuraux, E. Faudot, K. Crombé, V. Kyrytsya, J. Hillairet and M. Goniche, ,"Self-consistent radio-frequency wave propagation and peripheral direct current plasma biasing: Simplified three dimensional non-linear treatment in the 'wide sheath' asymptotic regime", *Phys. Plasmas* **19** (2012) 092505
8. [Colas 2017] L. Colas, L-F. Lu, A. Krivska, J. Jacquot, J. Hillairet, W. Helou, M. Goniche, S. Heuraux and E. Faudot, "Spatial proximity effects on the excitation of Sheath RF Voltages by evanescent Slow Waves in the Ion Cyclotron Range of Frequencies", *Plas. Phys. Cont. Fusion* **59** (2017) 025014
9. [Corre 2012] Y. Corre *et al*, "Characterization of heat flux generated by ICRH heating with cantilevered bars and a slotted box Faraday screen", *Nucl. Fusion* **52** (2012) 103010
10. [D'Ippolito 2006] D. A. D'Ippolito, J. R. Myra,"A radio-frequency sheath boundary condition and its effect on slow wave propagation", *Phys. Plasmas* **13** (2006) 102508
11. [D'Ippolito 2008] D. A. D'Ippolito, J. R. Myra, E.F. Jaeger and L.A. Berry, "Far-field sheaths due to fast wave incident on material boundaries", *Phys. Plasmas*. **15** (2008) 102501
12. [D'Ippolito 2013] D. A. D'Ippolito, J. R. Myra, R. Ochoukov and D. G. Whyte, "Modelling far-field radio-frequency sheaths in Alcator C-Mod", *Plas. Phys, Cont. Fusion*, **55** (2013) 085001
13. [D'Ippolito 2015] D. A. D'Ippolito and J. R. Myra, "A generalized BC for radio-frequency sheaths", *AIP Conf. Proc*. **1689** (2015), 050001
14. [Faudot 2013] E. Faudot, S. Heuraux, M. Kubic, J. Gunn and L. Colas, "Fluid modeling of radio frequency and direct currents in a biased magnetized plasma", *Phys. Plasmas* **20** (2013) 043514
15. [Heuraux 2015] S. Heuraux et.al, "Simulation as a tool to improve wave heating in fusion plasmas", *J. Plasma. Phys*. **81** (2015) 435810503
16. [Kohno 2012] H. Kohno, J. R. Myra and D. A. D'Ippolito, "A finite element procedure for radio-frequency sheath–plasma interactions in the ion cyclotron range of frequencies", *Comput. Phys. Commun*. **183** (2012) 2116-2127
17. [Kohno 2012A] H. Kohno, J. R. Myra and D. A. D'Ippolito, "Numerical analysis of radio-frequency sheath-plasma interactions in the ion cyclotron range of frequencies", *Phys. Plasmas* **19** (2012) 012508
18. [Kohno 2015] H. Kohno, J. R. Myra and D. A. D'Ippolito, "Numerical investigation of fast-wave propagation and radio-frequency sheath interaction with a shaped tokamak wall", *Phys. Plasmas*, **22** (2015) 072504
19. [Kubic 2013] M. Kubic, J. P. Gunn, S. Heuraux, L. Colas, E. Faudot, J. Jacquot, "Measurement of sheath potential in RF-biased flux tubes using a retarding field analyzer in Tore Supra Tokamak", *J .Nuc. Mat*. **438** (2013) S509-S512
20. [Jacquot 2012] J. Jacquot, D. Milanesio, L. Colas, S. Heuraux and M. Goniche, "Recent advances in self-consistent RF sheath modeling and related physical properties: Application to Tore Supra IC antennae",

Proc. 39th EPS Conf. & 16th Int. Congress on Plasma Physics (Stockholm, Sweden, 2-6 July 2012) Poster P2.038
21. [Jacquot 2013] J. Jacquot, L. Colas, F. Clairet, M. Goniche, S. Heuraux, J. Hillairet, G. Lombard and D. Milanesio, "2D and 3D modelling of wave propagation in cold magnetized plasma near the Tore Supra ICRH antenna relying on the perfectly matched layer technique", *Plas. Phys. Cont. Fusion* **55** (2013) 115004
22. [Jacquot 2014] J. Jacquot, D. Milanesio, L. Colas, Y. Corre, M. Goniche, J. Gunn, S. Heuraux, M. Kubic and R. Maggiora, "Radio-frequency sheaths physics: Experimental characterization on Tore Supra and related self-consistent modeling", *Phys. Plasmas* **21** (2014) 061509
23. [Jacquot 2015] J. Jacquot et.al, "Full wave propagation modelling in view to integrated ICRH wave coupling/RF sheaths modelling", *AIP Conf. Proc*, **1689** (2015) 050008
24. [Langmuir 1913] I. Langmuir, "The effect of space charge and residual gases on thermionic currents in high vacuum", *Phys. Rev*. **2** (1913) 450
25. [Louche 2015] F. Louche *et al*, "Designing the IShTAR antenna: Physics and engineering aspects", *AIP Conf. Proc*, **1689** (2015) 070016
26. [Lu 2016] L. Lu, K. Crombe, D. Van Eester, L. Colas, J. Jacquot and S. Heuraux, "Ion cyclotron wave coupling in the magnetized plasma edge of Tokamaks: impact of a finite, inhomogeneous density inside the antenna box", *Plas. Phys. Cont. Fusion*, **58** (2016) 055001
27. [Mendes 2010] A. Mendes, L. Colas, K. Vulliez, A. Ekedahl, A. Argouarch and D. Milanesio, "Reduction of RF-sheaths potentials by compensation or suppression of parallel RF currents on ICRF antennas", *Nucl. Fusion*, **50** (2010) 025021
28. [Moritz 2016] J. Moritz, E. Faudot, S. Devaux and S. Heuraux, "Plasma sheath properties in a magnetic field parallel to the wall", *Phys. Plasmas* **23** (2016) 062509
29. [Ochoukov 2014] R. Ochoukov *et al*, "ICRF-enhanced plasma potentials in the SOL of Alcator C-Mod", *AIP Conf. Proc*. **1580** (2014) 267 and *Plas. Phys, Cont. Fusion* 56 (2014) 015004
30. [Perkins 1989] F. W. Perkins, "Radiofrequency sheaths and impurity generation by ICRF antennas", *Nucl. Fusion*, **29** (1989) 583
31. [Smithe 2015] D. N. Smithe, T. G. Jenkins and J. R. King, "Improvements to the ICRH antenna time-domain 3D plasma simulation model", *AIP Conf. Proc*. **1689** (2015) 050004
32. [Spitzer 1953] L. Spitzer and R. Harm, "Transport phenomena in a completely ionized gas", *Phys. Rev*. **89** (1953) 977
33. [Stangeby 2000] P.C. Stangeby, "The Plasma Boundary of Magnetic Fusion Devices", Plasma Physics Series, IoP Publishing Ltd, Bristol, UK (2000)
34. [Stangeby 2012] P. C. Stangeby, "The Chodura sheath for angles of a few degrees between the magnetic field and the surface of divertor targets and limiters", *Nucl. Fusion*, **52** (2012) 083012
35. [Stix 1992] T. H. Stix, "Waves in plasmas", 1992, AIP Press
36. [Tamain 2016] P. Tamain, C. Colin , L. Colas, C. Baudoin, G. Ciraolo, R. Futtersack, D. Galassi , Ph. Ghendrih, N. Nace, F. Schwander and E. Serre, "Numerical analysis of the impact of an RF sheath on the Scrape-Off Layer in 2D and 3D turbulence simulations", proc. 22nd International Conference on Plasma Surface Interactions in Controlled Fusion Devices, Poster P.2.48 Nuclear Materials and Energy in press doi: http://dx.doi.org/10.1016/j.nme.2016.12.022
37. [Van Eester 2015] D. Van Eester and K. Crombé, "A crude model to study radio frequency induced density modification close to launchers", *Phys. Plasmas* **22** (2015) 122505
38. [Zhang 2015] X. J. Zhang and F. W. Yao, "Optimization study of ICRF hydrogen minority heating in a deuterium plasma of EAST", *Plas. Sci & Tech*, **6** (2015) 454
39. [Zhang 2016] W. Zhang, V. Bobkov, T. Lunt, J.-M. Noterdaeme, D. Coster, R. Bilato, P. Jacquet, D. Brida, Y. Feng and E.Wolfrum, "3D simulation of gas puff effects on edge density and ICRF coupling in ASDEX Upgrade", *Nucl. Fusion*, **56 (**2016) 036007